

Elucidating Li₅NCl₂: A fully-reduced, highly-disordered nitride- halide electrolyte for solid state batteries with lithium metal anodes

Victor Landgraf^a, Theodosios Famprakis^a, Swapna Ganapathy^a, Lars Bannenberg^a, Joris de Leeuw^a
Marnix Wagemaker^{a*}

^a Faculty of Applied Sciences, Delft University of Technology, 2628 Delft, The Netherlands

*m.wagemaker@tudelft.nl

Abstract

Solid electrolytes that are thermodynamically stable against lithium metal may be key to stabilizing lithium metal/solid electrolyte interfaces which is crucial for realizing all solid state batteries that outperform conventional lithium ion batteries. In this study we investigate Li₅NCl₂ (LNCl) a fully-reduced solid electrolyte that is thermodynamically stable against lithium metal. Combining experiments and simulations we investigate the lithium diffusion mechanism, different synthetic routes and the electrochemical stability window of LNCl. Li nuclear magnetic resonance (NMR) experiments show that fast Li motion ($\sigma_{RT} > 0.1 \text{ mS cm}^{-1}$) is present in LNCl which is however not accessible in macroscopic LNCl pellets. Our ab-initio calculations indicate a disorder-induced wide spread of different lithium jumps in LNCl with certain jumps being much more diffusion limiting than others providing an explanation for the discrepancies in the NMR and electrochemical impedance spectroscopy (EIS) conductivity measurements. The fundamental understanding of the diffusion mechanism we develop herein will guide future synthesis optimizations for LNCl to further improve its conductivity (currently $\sigma_{RT} = 0.015 \text{ mS cm}^{-1}$) and may be applied to other highly-disordered fully-reduced antifluorite electrolytes. We further find that the previously reported anodic limit (>2V vs Li+/Li) is an overestimate and find the true anodic limit at 0.6 V which is in close agreement with our first-principles calculations. Because of LNCl's stability against lithium metal we identify LNCl as a prospective artificial protection layer between highly-conducting solid electrolytes and strongly-reducing lithium metal anodes; Thus we also provide an investigation of the chemical compatibility of LNCl with common highly-conducting solid electrolytes.

Introduction

Conventional lithium-ion batteries are reaching their theoretical limits in term of energy density and rely on flammable liquid electrolytes.^{1 2} A promising alternative for the next generation of energy storage device are all-solid-state batteries (ASSBs), which may enable the next step-up in terms of energy density and safety required for the ongoing energy transition and the electrification of transport.^{2 3}

Numerous solid electrolytes (SEs) have been developed, reaching Li-ion conductivities of up to 10^{-2} S cm⁻¹, are comparable with liquid electrolytes.^{4 5} However, the interfacial stability of SEs with both lithium metal (LM) and common high-voltage cathodes remains a tremendous challenge and hampers their application in ASSBs.^{6 7 4} A LM anode may be indispensable for ASSBs to surpass conventional lithium-ion batteries in terms of energy density³ thus stable LM/SE interfaces are crucial for the full-scale commercialization of ASSBs.

The stability of the LM/SE interface can be separated into two inter-linked properties: chemical and contact stability. Chemical stability may potentially be achieved in two ways. (i) In the simplest case, the SE is thermodynamically stable against LM and no interphase is formed. (ii) If the SE is thermodynamically unstable against LM, chemical stability can be achieved if it decomposes into an electronically insulating and ion conducting interphase, self-limiting further decomposition and thus effectively serving as a passivation layer^{4 8} Such interphases, however, may lead to inhomogeneous Li plating which favors the growth of lithium dendrites and cell short-circuiting. Additionally, volume changes during decomposition may incite contact losses.⁶ It was previously believed that SEs could inhibit the growth of Li dendrites due to their high stiffness (large elastic moduli) compared to LM.⁹ This assumption has now been refuted theoretically¹⁰ and experimentally.^{11 12} Recently, the crucial role of microstructural aspects to inhibit Li dendrite growth has also been established.² This convoluted interplay of mechanical and microstructural properties, dendritic growth, (electro)chemical and contact stability renders the designing of stable LM/SE interfaces a difficult task. Uncontrollable SE decomposition at the LM/SE interface poses an additional engineering challenge and motivates the investigation of SEs that are thermodynamically stable against LM as they may facilitate the LM/SE interface.

In search of new SEs, researchers investigated the compositional space between Li₃N and LiX (X=Cl,Br,I).¹³ As Li₃N and the LiX salts are thermodynamically stable against LM all members on the quasi-binary Li₃N-LiX phase cuts were equally expected to be stable against LM. The numerous new phases discovered are

called lithium nitride-halides. Cubic LNCl which crystallizes in the antifluorite structure emerged as the best lithium-ion conducting lithium nitride halide ($\sigma_{\text{RT}} = 1 \cdot 10^{-3} \text{ mS cm}^{-1}$),¹³ demonstrating excellent (electro)chemical stability against LM, an anodic limit of $>2 \text{ V}$ (vs Li⁺/Li) and low electronic conductivity of $<1 \cdot 10^{-10} \text{ S cm}^{-1}$.¹³ Marx and coworkers revisited numerous lithium nitride halides, better refined their structures and often corrected the initially reported stoichiometries.^{14 15 16 17} LNCl was found to have a stoichiometry of Li_5NCl_2 , not $\text{Li}_9\text{N}_2\text{Cl}_3$.¹⁵ Thereafter, LNCl was not revisited until Galvez-Aranda and Seminario investigated the solid-solid LM/LNCl interface with ab-initio molecular dynamics (AIMD) simulations and confirmed the stability of the interface.¹⁸ Sang and coworkers recently performed an ab-initio high-throughput investigation and identified new lithium nitride halide phases that may potentially be synthesizable and of which some are predicted to be highly Li-ion conducting ($>10^4 \text{ S cm}^{-1}$).¹⁹

LNCl crystallizes in the antifluorite structure with the Fm-3m space group. N/Cl partially occupy the (0,0,0) site with a 1:2 ratio (Figure 1a).¹⁵ The tetrahedral interstitials (0.25, 0.25, 0.25) site are partially occupied by lithium ions (82.5 %) and LNCl thus features a partially occupied lithium sub-lattice which is a good predisposition for high lithium-ion conductivity.²⁰ Reinvestigating materials with promising structural features recently led to the discovery of high ionic conductivities in materials that were thought to be poorly conducting. Lithium halide ceramics with trivalent metals (Li_3MX_6 , M=Y, Er, Zr, In...; X = Cl, Br, I), for example, had been known for decades.²¹ However, their high ionic conductivities were only discovered after Asano and coworkers in 2018 first demonstrated that ionic conductivities in the range of 0.03-1.7 mS cm^{-1} could be obtained for Li_3YCl_6 and Li_3YBr_6 via a mechanochemical synthesis route.^{22 23} In contrast, reinvestigating the electrochemical stability window of SEs, showed that previously reported stability windows were frequently too large; the stability window of SEs was systematically overestimated because of the use of semi-blocking electrodes that provide poor contact at the SE/electrode interface.^{24 25}

In view of the above and because of its excellent stability against LM it is due time to reinvestigate LNCl. Combining experiment and calculation we investigate (i) the fundamental bulk ion-conduction mechanism in LNCl, (ii) the effects of mechanochemical treatments on LNCl and (iii) its anodic limit. Based on our findings we reassess the applicability of LNCl for ASSBs.

Results and Discussion

Computational investigation of Li diffusion in LNCl. LNCl is a material with partial occupancies and constructing a 2x2x2 supercell that can be used in ab initio \simulations necessitates the probing of different possible atom arrangements. Inspired by references²⁶ and²⁷ we obtained a model supercell of

LNCI by a combination of electrostatic energy minimization and the screening >10,000 atom arrangements. We adopted the supercell with the lowest internal energy as our model LNCI supercell. Our model supercell is slightly distorted from cubic symmetry (Table S1) which is likely a consequence of the limited size of our model supercell. Similar distortions from cubic symmetry of an LNCI supercell have been observed in a previous computational investigation (Table S1) of LNCI.¹⁸ Overall, good agreement is found between the unit cell parameters measured from Rietveld refinement of X-ray diffraction (XRD) data and our model supercell (Table S1). The side lengths of the supercell deviate by at most 2.5% and the supercell volume and density differ by less than 0.6% from experiments (Table S1). In LNCI the Li sites are enclosed by tetrahedra composed of nitride and chloride ions. The tetrahedra are composed of either 1 nitride and 3 chlorides (from here on referred to as a Cl_3N_1) site), 2 nitrides and 2 chlorides (Cl_2N_2), 3 nitride and 1 chlorides (Cl_1N_3), 4 chlorides (Cl_4) or 4 nitrides (N_4). In mixed N/Cl tetrahedra we found that Li was displaced from the center of the tetrahedron towards the nitride ions (Figure S1). Figure 1e shows the radial-distribution function (RDF) of the Li-N and Li-Cl distances throughout an ab-initio molecular dynamics (AIMD) simulation. The Li-N peak in Figure 1e appears at shorter radii than the Li-Cl peak suggesting that a shorter Li-N distance is maintained not only in the fully relaxed state at 0 K (Figure S1) but also during diffusion between sites throughout the AIMD simulation. Figures 1b and 1c are lithium density maps of our AIMD simulations at 910 K. The density maps show that Li diffuses through the shared edge of two neighboring tetrahedra. The density maps also reveal that the Li-density through shared-edges composed of two chloride ions (Cl-Cl edges, red highlighting in Figure 1b) is lower than through Cl-N and N-N edges. This suggests that diffusion through N-N and Cl-N edges is more favorable than through Cl-Cl edges.

As done in previous studies,^{28 29} we dissected our AIMD simulations into individual jumps between lithium sites. This enabled us to estimate the average attempt-frequency v^* in LNCI ($1.08 \cdot 10^{13}$ Hz) and the jump frequency between different sites $v_{A \rightarrow B}$ as explained in detail elsewhere.²⁸ The activation energy for a jump event was estimated with the following expression:

$$E_{a,A \rightarrow B} = -k_b T \ln \left(\frac{v_{A \rightarrow B}}{v^*} \right) \quad (1)$$

where k_b is Boltzmann's constant, T the temperature in K and $E_{a,A \rightarrow B}$ the activation energy of a generalized jump event from site A to site B. We would like to highlight that a site-independent, isotropic attempt frequency of $1.08 \cdot 10^{13}$ Hz is assumed. $E_{a,jump}$ calculated with equation 1 can thus not be interpreted as the actual energy-barrier for diffusion between two sites. $E_{a,jump}$ should rather be interpreted as a metric

for the affinity for jumps between two sites. The affinity for jumps between two sites is also represented by the jump frequency $v_{A \rightarrow B}$ but we favor the use of $E_{a, \text{jump}}$ over $v_{A \rightarrow B}$, because $v_{A \rightarrow B}$ is temperature dependent. The temperature dependence of $v_{A \rightarrow B}$ is moderated by the temperature term T in equation 1, making $E_{a, \text{jump}}$ a temperature-independent metric for the affinity for jumps between two sites.

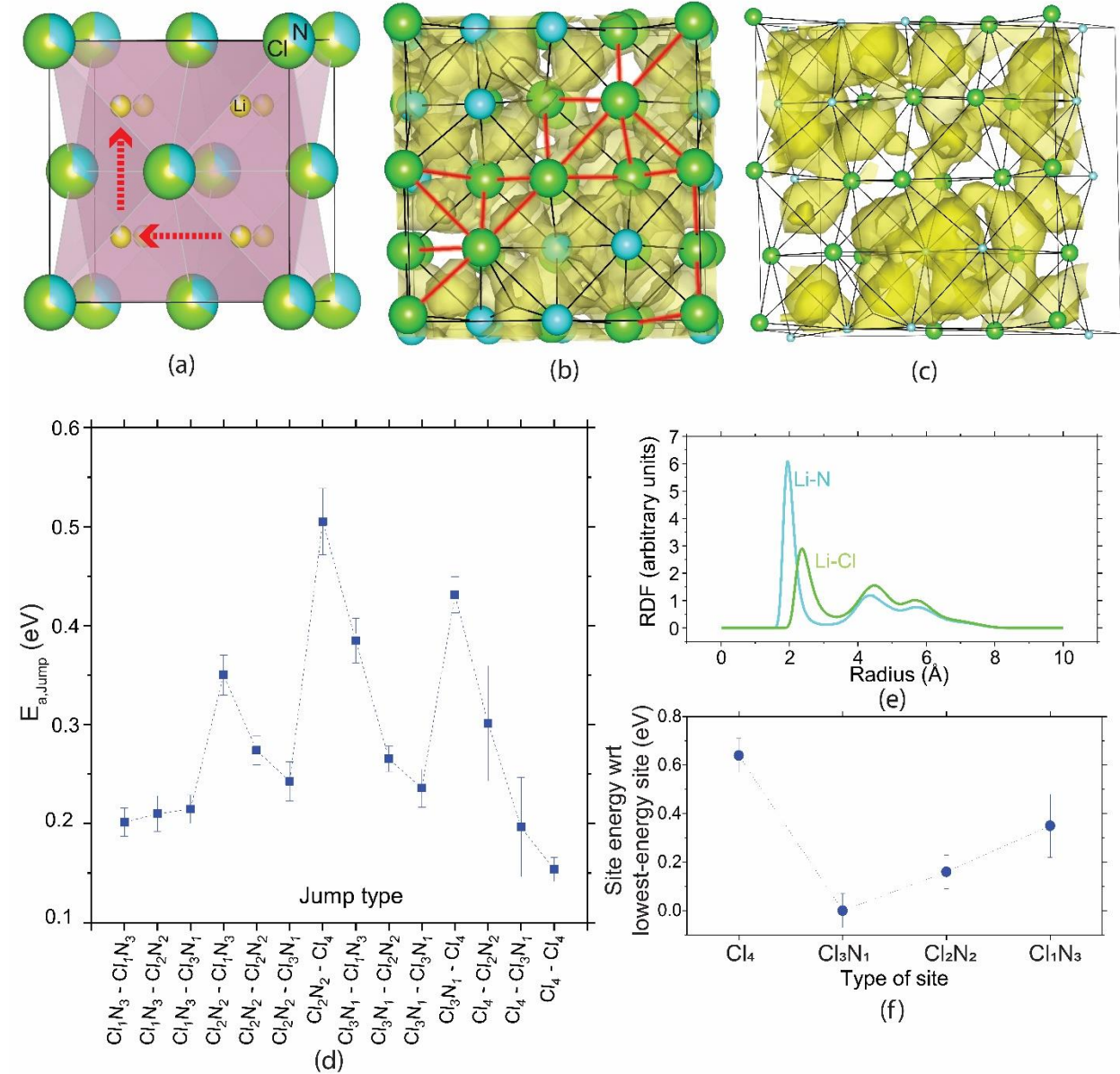


Figure 1. a) Unit cell of LNCl. The green and turquoise spheres represent Cl and N, respectively. The red arrows schematically show the Li diffusion pathways in LNCl. b) LNCl supercell with the Li density maps obtained from an AIMD simulation at 910 K. The tetrahedra surrounding Li sites are shown as black lines and edges composed of two chlorides (Cl-Cl) are highlighted in red. c) Same supercell as in b). For better readability only one layer is shown, the supercell is slightly turned and the N/Cl ions are made smaller. d) $E_{a,\text{jump}}$ for different Li jumps. The average $E_{a,\text{jump}}$ values and their respective standard errors plotted here are obtained

from 7 AIMD simulations at 910 K, 860 K, 800 K, 720 K, 700 K, 680 K 650 K, respectively. e) The RDFs obtained from an AIMD simulation at 910 K. f) Relative energies of the different Li-sites as obtained from the Li vacancy displacements to different sites.

Figure 1d shows the activation energy $E_{a,\text{jump}}$ for individual jump events in LNCl. The $E_{a,\text{jump}}$ values in LNCl span a wide range from 0.2 to 0.5 eV and it becomes apparent that jumps originating from Cl_2N_2 and Cl_3N_1 sites towards Cl_4 sites show particularly high $E_{a,\text{jump}}$ values (>0.4 eV). Figure 1f shows the energy differences between the Li sites. This energy difference between Li sites was obtained by displacing a Li ion in a site A to a vacant site B. We then interpreted the energy difference between the two supercells as the energy difference between sites A and B. It becomes apparent that Cl_4 sites are >100 meV higher in energy than all other sites. The large $E_{a,\text{jump}}$ values for $\text{Cl}_2\text{N}_2 \rightarrow \text{Cl}_4$ and $\text{Cl}_3\text{N}_1 \rightarrow \text{Cl}_4$ jumps thus likely originate from the large site-energy differences between $\text{Cl}_2\text{N}_2/\text{Cl}_3\text{N}_1$ and Cl_4 sites.

In LNCl Li diffuses through the edge of edge-sharing tetrahedra and thus diffuses through bottleneck (BN) edges that are composed of either two chlorides (Cl-Cl), one chloride and one nitride (Cl-N) or two nitrides (N-N). To deconvolute the effects of the jump type ($\text{Cl}_2\text{N}_2 \rightarrow \text{Cl}_3\text{N}_1$, $\text{Cl}_2\text{N}_2 \rightarrow \text{Cl}_2\text{N}_2$, ...) and of the BN composition on $E_{a,\text{jump}}$ we focused on jumps between the same type of sites through different BN compositions (Table 1). Examining jumps between Cl_3N_1 and Cl_2N_2 sites, respectively, we found that the more nitrogen the BN contains, the lower $E_{a,\text{jump}}$ (Table 1). This observation suggests that the $E_{a,\text{jump}}$ values are affected by an intrinsic characteristic of the BN.

BN size is often considered to influence the activation barrier.^{20 30 31} We define the bottleneck size in LNCl as such:

$$R_b = R_{A,B} - (r_A + r_B) \quad (2)$$

where $R_{A,B}$ is the distance between the peripheral atoms and r_A and r_B the ionic radii of the peripheral ions A and B. In the optimal case, R_b should be equal to the diameter of Li^+ which is 1.18 Å.^{20 32} If the bottleneck is too large or too small, thermal energy may be required to adjust the bottleneck size, which increases the activation energy for a jump process.²⁰ Using the Shannon radii³² of Cl^- and N^{3-} we calculated the R_b for Cl-Cl, Cl-N and N-N bottlenecks to be 0.10 Å, 0.50 Å and 0.72 Å. In each case R_b is smaller than 1.18 Å and thermal energy is likely required to open the bottleneck for Li^+ diffusion. Interestingly, the Cl-Cl BN with (for a fixed jump type) the largest $E_{a,\text{jump}}$ has a R_b that is furthest from the optimum and the N-N BN with (for a fixed jump type) the lowest $E_{a,\text{jump}}$ has a R_b that is closest to the optimum. Bottleneck size could thus provide an explanation for the $E_{a,\text{jump}}$ dependence on BN composition. We conclude from Table 1 that for the same jump type, altering the BN composition affects $E_{a,\text{jump}}$. In contrast, for the same BN

composition, $E_{a,jump}$ varies for different jump types. Thus, $E_{a,jump}$ depends in a convoluted manner on both, the jump type and the BN composition.

Table 1. $E_{a,jump}$ values for jumps between equal sites through different types of bottlenecks and the average of all types of jumps through different types of bottlenecks.

Type of jump	$E_{a,jump}$ through different bottlenecks (eV)		
	Cl-Cl	Cl-N	N-N
Cl ₃ N ₁ -> Cl ₃ N ₁	0.41 ± 0.03	0.23 ± 0.01	-
Cl ₂ N ₂ -> Cl ₂ N ₂	0.43*	0.34 ± 0.02	0.21 ± 0.01
Cl ₁ N ₃ -> Cl ₁ N ₃	-	-	0.18 ± 0.01
Cl ₄ -> Cl ₄	0.13 ± 0.01	-	-
Average of all types of jumps	0.32 ± 0.02	0.27 ± 0.01	0.22 ± 0.01

Note: The averages and their respective standard errors listed in this table are obtained from three AIMD simulations at 910 K, 860 K and 800 K. Cl₂N₂ -> Cl₂N₂ jumps through Cl-Cl bottlenecks were only observed at 910 K and only between one of the two Cl₂N₂ -> Cl₂N₂ site pairs that are connected by a Cl-Cl bottleneck (Table S5) which is why we do not report a standard error for this value (marked with *).

From AIMD simulations of LNCl at different temperatures, we obtained the tracer diffusivity (D_{tr}) at different temperatures which enables the estimation of an activation energy (Figure S2) as done in previous studies.³³ The ion conductivity σ can be obtained from the diffusivity using the Nernst-Einstein equation³³:

$$\sigma = \frac{n(ze)^2}{k_b T H_R} D_{tr}. \quad (3)$$

where n and z are the number density of charge carriers and the charge of the charge carrier as a multiple of the elementary charge e , respectively. We assumed a Haven ratio H_R of 1. Our tracer-diffusivity analysis predicts an activation energy of 0.35 ± 0.03 eV and a conductivity of 0.3 mS cm^{-1} at 300 K for LNCl. Dissecting our AIMD simulations into individual jump events enabled the estimation of the jump-diffusivity D_J which can be obtained from the Einstein-Smoluchowski equation^{28 34}

$$D_J = \frac{1}{N^2 dt} \sum_{i=1}^M a_{A \rightarrow B}^2 \quad (4)$$

where N is the total number of diffusing ions, d the dimensionality of diffusion, t the total simulation time, M the total number of jumps observed and $a_{A \rightarrow B}$ the jump distance of a generalized jump-event. From D_J the conductivity can be estimated by inserting D_J into equation 3 instead of D_{tr} . Our jump-diffusivity analysis predicts an activation energy of 0.27 ± 0.01 eV and a conductivity of 4.1 mS cm^{-1} at 300 K. Conductivities derived from D_J are typically larger than conductivities derived from D_{tr} because every jump is assumed to contribute to macroscopic diffusion. However, “back and forth” jumps between two sites and locally confined diffusion do not effectively contribute to macroscopic diffusion and thus tracer diffusivities better describe macroscopic bulk diffusion.

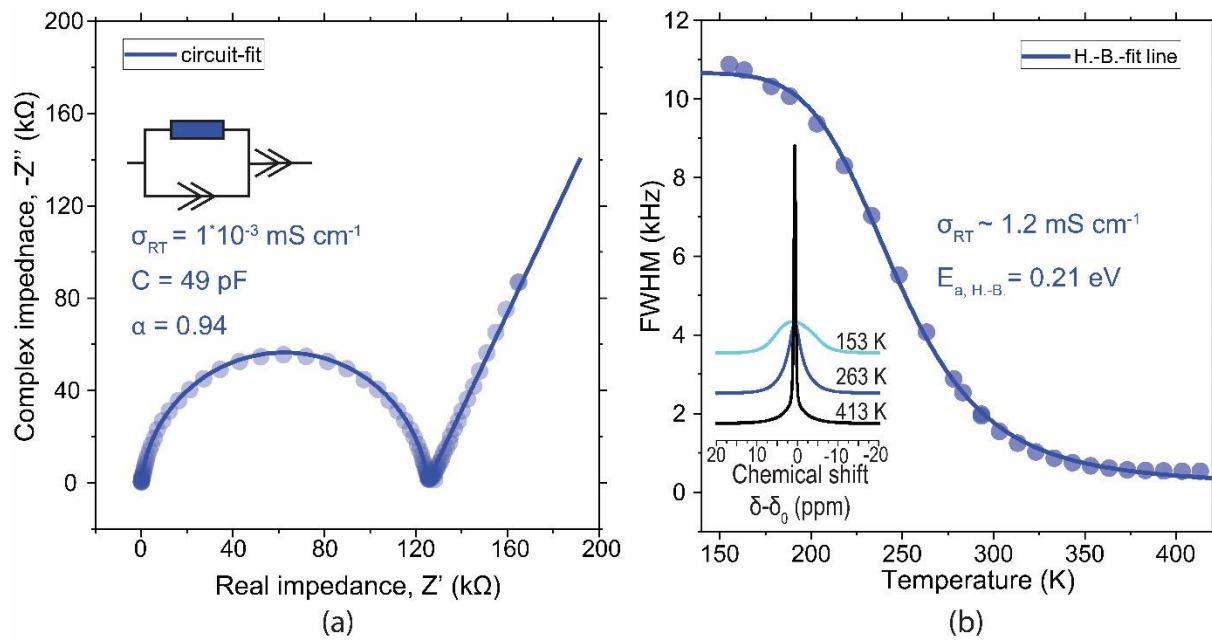


Figure 2. a) Nyquist plot of LNCl-I at RT. Experiments were done in a SS|LNCl-I|SS cell (SS=stainless steel). The inset shows the equivalent circuit. b) FWHM of the ${}^7\text{Li}$ NMR signal of LNCl at different temperatures. The inset shows the NMR signal at three distinct temperatures. The solid line is the fit obtained from the Hendrickson-Bray equation.

Experimental investigation of Li conductivity in LNCl. We synthesized LNCl via a solid-state synthesis route by heating stoichiometric amounts of LiCl and Li₃N at 600°C for 3h and subsequent air quenching as following in ref ³⁵. LNCl synthesized in this way is from now on referred to as LNCl-I. The lattice constants previously reported for LNCl range from 5.386 Å to 5.416 Å.^{36 15 37} This variation in the lattice parameter may be a consequence of the different annealing protocols employed for LNCl synthesis in refs. 15,³⁶ and ³⁷. Also the exact quenching procedure is not described in detail in refs. ³⁶ and ³⁷. The lattice constant 5.396 Å that we determined from our XRD Rietveld refinements (Figure S3, Table S1) for LNCl fits well into the range of lattice parameters determined in previous studied (5.386 Å to 5.416 Å).^{15 36 37} The purity of

LNCI-I was verified by XRD and no impurities were observed (Figure S3). Figure 2a shows the electrochemical impedance spectrum (EIS) Nyquist plot of LNCI-I at room temperature (RT). The impedance of LNCI-I could be fitted with a resistor (R) parallel to a constant phase element (CPE). The effective capacitance of the CPE calculated with Brug's formula^{38 39} is 49 pF which is a value typically associated with ion conduction in the bulk of solid ion conductors.⁴⁰ A prominent secondary process in the impedance that may for instance arise from grain boundaries was not observed even at -30°C (Figure S4). We thus interpret the impedance of LNCI-I at RT as bulk dominated. We calculated the ionic conductivity of LNCI to be $1 \cdot 10^{-3}$ mS cm⁻¹ at RT, which comparable with previous reports.¹³ The activation energy measured from temperature dependent impedance spectroscopy was 0.471 ± 0.005 eV which is close to the value of 0.49 eV previously reported for LNCI.¹³

Complimentary to EIS, Li NMR provides insights on Li diffusion in ion conductors.⁴¹ Figure 2b shows the ⁷Li NMR signal linewidth evolution with increasing temperature for LNCI-I and the typical line shape narrowing profile was observed.^{41 42 43} The activation energy of the diffusion process that inflicts the line-narrowing can be obtained from the phenomenological equation derived by Hendrickson and Bray (H.-B.)⁴³:

$$\Delta v(T) = \Delta v_R \left[1 + \left(\frac{\Delta v_R}{B} - 1 \right) \exp \left(-\frac{E_a}{k_b T} \right) \right]^{-1} + D \quad (5)$$

where $\Delta v(T)$ is the linewidth at temperature T, and Δv_R is the linewidth in the rigid-lattice regime. B is the linewidth that would be obtained at extreme narrowing in the absence of magnetic field inhomogeneity and D is a correction factor accounting for broadening arising from the inhomogeneity of the static magnetic field. From this model we obtain an activation energy of 0.21 ± 0.01 eV for lithium diffusion in LNCI. The value of B is an indicator for the 'range' of motion. The larger B, the more 'short-range' the motion because locally confined motion is not expected to entirely eliminate dipole-dipole interactions.⁴³ For different ion conductors values for B ranged from 10^{-3} to 10^{-13} kHz.⁴³ The value of B obtained for LNCI ($5 \cdot 10^{-4}$ kHz) thus suggests that the line-narrowing is caused by locally confined motion.⁴³ To what range exactly this motion may be confined, goes beyond the predictive scope of the Hendrickson-Bray equation.

An additional estimate of the activation energy can be obtained from the empirical expression of Waugh and Fedin (W.-F.)⁴⁴:

$$E_a^{WF} = 1.617 \cdot 10^{-3} \frac{T_c}{K} \quad (6)$$

where T_c is the onset temperature of motional narrowing in Kelvin. A drawback of the W.-F. approach is the difficulty to estimate the exact onset of motional narrowing. We observe the onset of narrowing at ~180 K and from the W.-F. expression we obtain an activation energy of 0.29 eV. Generally, $^{6,7}\text{Li}$ NMR-measurements also capture Li motion that does not effectively contribute to macroscopic diffusion such as locally-confined diffusion and “back and forth” jumps. Activation energies obtained from D_j values thus better match activation energies obtained from $^{6,7}\text{Li}$ NMR-measurements than activation energies obtained with D_{tr} values. The activation energies obtained from the H.-B. and the W.-F. expressions and the activation energy obtained from the D_j values in our AIMD simulations are all in a range between 0.21 eV and 0.29 eV (Table 2). Generally, at temperatures below the onset of line narrowing the jump frequency is lower than the rigid-lattice-regime NMR line width.⁴¹ At temperatures where narrowing is observed the jump frequency is higher than the rigid-lattice-regime NMR line width.⁴¹ When extrapolating the jump frequencies obtained from AIMD simulations to temperatures of the rigid-lattice regime (<150 K) we indeed obtain jump frequencies lower than the rigid-lattice-regime NMR line width of 10 kHz. Extrapolating the jump frequencies obtained from AIMD simulations to temperatures of narrowing (>180 K) we obtain jump frequencies > 100 kHz and thus much larger than the rigid-lattice-regime NMR line width. We thus observe reasonable agreement between our AIMD simulations and NMR measurements.

The activation energies obtained from NMR can be used to calculate the Li conductivity at 300 K in LNCI as follows⁴¹:

$$\sigma = \frac{fn(ze)^2a^2}{6k_bT} v^* \exp\left(\frac{-E_a}{k_bT}\right) \quad (7)$$

where a is the average jump distance taken as 2.7 Å which is the average distance between Li sites in LNCI and f is the correlation factor; the correlation factor is a measure for how efficiently jumps contribute to macroscopic diffusion and can be calculated from the ratio D_{tr}/D_j .²⁸ From the extrapolated values of D_{tr} and D_j at 300 K we obtained a correlation factor $f=0.06$.

Using the range of activation energies obtained from the linewidth narrowing (0.21-0.29 eV), the correlation factor ($f = 0.06$) and assuming an attempt frequency v^* of $1 \cdot 10^{13}$ Hz, a range for the ion conductivity at 300 K as probed by ^7Li NMR was calculated (Table 2).

Table 2. Ion Conductivity and Ea obtained by different methods.

Method	E _a (eV)	σ _{RT} (mS cm ⁻¹)	Length scale probed
		[lower boundary; upper boundary]	
AIMD _{Tracer}	0.35 ± 0.03	0.3 [0.07; 1.2]	10 Å
AIMD _{Jump}	0.27 ± 0.01	4.9 [4.4; 5.5]	10 Å
⁷ Li NMR signal line shape narrowing	0.25 [0.29; 0.21]	1.2 [0.18; 6.9]	<500 μm
EIS	0.471 ± 0.005	1.0 ·10 ⁻³	~500 μm

Note: The lower and upper boundaries for σ_{RT} are obtained by using the respective extremes of the E_a values for extrapolation (e.g. 0.32 and 0.38 eV in the case of AIMD_{Tracer}). For ⁷Li NMR line shape narrowing the lower and upper boundaries originate from the different E_a values obtained from different models.

Table 2 summarizes the activation energies and RT conductivities obtained from different techniques. We observe reasonable agreement between our NMR measurements and the jump-analysis of our AIMD simulations (Table 2). The activation energy obtained from the tracer-analysis of our AIMD simulations is 0.08 eV larger than that of the jump-analysis. This is most likely a consequence of the difference in how the mean square displacement is calculated (see Methodology) which may affect the respective temperature dependence of D_j and D_{tr}. Diffusivities obtained from the jump-analysis (D_j) tend to be overestimates because the jump-analysis captures locally confined motion that does not effectively contribute to macroscopic diffusion. Activation energies and conductivities obtained from the tracer-analysis (D_{tr}) of AIMD simulations thus better compare to the bulk properties of materials measured by EIS. Interestingly, the activation energy obtained from EIS is by 0.1 eV larger than the activation energy obtained from our AIMD tracer analysis. We would like to bring forward two conceivable explanations for this discrepancy. (i) The length scale probed by EIS is 5 orders of magnitude larger than the one probed in our AIMD simulations (Table 2). EIS may potentially capture a diffusion limitation occurring at the mesoscale of our LNCl pellets. Such a diffusion limitation may for example arise from potential amorphous impurities in our LNCl pellets that would not be detected by XRD. (ii) A second explanation for the discrepancy between our AIMD tracer-analysis and our EIS experiments may be diffusion limiting Cl₄ sites and/or Cl-Cl edges in the bulk of our LNCl pellets: Our AIMD analysis shows a poor affinity for jumps through Cl₄-sites and Cl-Cl edges (E_{a,jump}>0.4 eV). In our model LNCl supercell (side length 10 Å) the Li

diffusion pathways are not limited by Cl_4 sites and/or Cl-Cl edges. However, with EIS we capture effects at the scale of our polycrystalline LNCI pellets (thickness $\sim 500 \mu\text{m}$). Between different crystallites the distribution of the Li sites likely varies and the likelihood of diffusion-limiting Cl_4 sites and/or Cl-Cl bottlenecks increases and may restrict the macroscopic conductivity, measured by EIS.

Mechanochemical treatment of LNCI. It has been repeatedly demonstrated that mechanochemical processing can dramatically improve the ion conductivity of inorganic ceramics.²³⁻⁴²

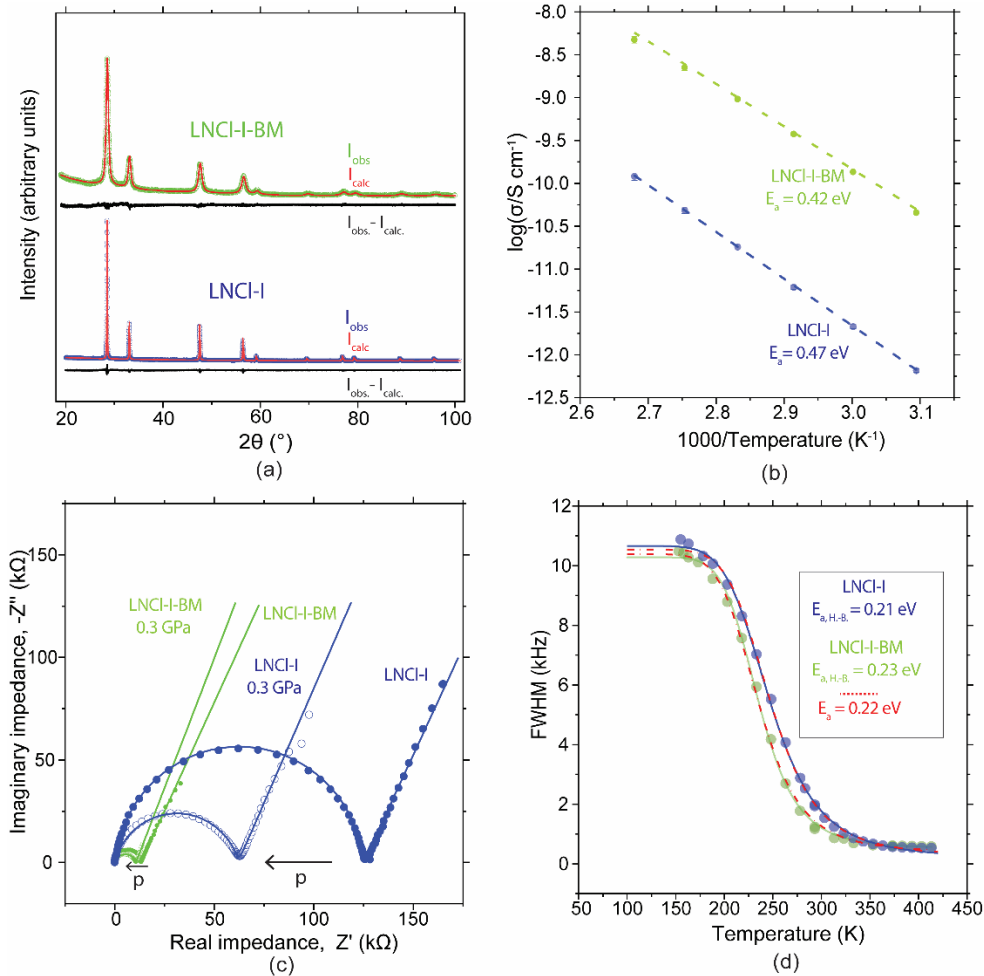


Figure 3. a) XRDs of LNCI-I and LNCI-I-BM with Rietveld refinements and the difference profile. b) Arrhenius fits of the conductivities obtained at different temperatures from EIS for LNCI-I and LNCI-I-BM. The individual points are the averages of three measurements, error bars are smaller than the point symbol and therefore not visible. c) Nyquist plot of LNCI-I and LNCI-I-BM with and without pressure applied during measurement. d) ${}^7\text{Li}$ NMR signal line shape evolution with temperature for LNCI-I and LNCI-I-BM, the solid lines are the H.-B. fits, the red dashed lines are obtained from H.-B. fits with E_a as a fixed parameter set to 0.22 eV.

To investigate potential benefits of mechanical milling we processed LNCI-I for 4h in a planetary ball mill after solid-state synthesis. Samples prepared in this way are from now on referred to as LNCI-I-BM. LNCI-I remains stable during the milling as no impurity peaks are detected in the XRD of LNCI-I-BM. The XRD of LNCI-I-BM shows dramatic peak-broadening compared to LNCI-I (Figure S5). Rietveld refinements show that the lattice parameter of LNCI-I is decreased from 5.39(6) Å to 5.37(6) Å after the mechanical milling process. Additionally, Williamson-Hall analysis (Figure S6) shows that after milling the average crystallite size is dramatically reduced from the μm range to \sim 60 nm. Milling also imposes significant strain on the LNCI lattice so that we obtain a residual microstrain of $\epsilon = 1.04\%$ for LNCI-I-BM.

Interestingly, EIS shows that the ion conductivity of LNCI increases by an order of magnitude after milling reaching 0.01 mS cm^{-1} . Additionally, fits of the conductivities at different temperatures to Arrhenius' law (Figure 3b) show that the (macroscopic) E_a of LNCI-I is decreased from $0.471 \pm 0.005\text{ eV}$ to $0.426 \pm 0.005\text{ eV}$ after milling. As the crystallite size of LNCI-I-BM is substantially smaller, a larger volume fraction of grain boundary regions is expected in LNCI-I-BM as compared to non-BM LNCI. However, the EIS of LNCI-BM-4h could be excellently fitted with a single R-CPE with an effective capacitance of \sim 40 pF. As for LNCI-I we thus interpret the impedance in LNCI-I-BM to be bulk dominated. Longer milling of LNCI-I, for 8h and 12h did not further increase the conductivity and no significant further decrease of the crystallite size was obtained (Figure S6).

Reduced particle size is a proposed explanation for the improved ion conductivity in mechanically processed materials.^{45 46} Under the same pelletization conditions a smaller particle size facilitates compression and consolidation which improves the area-contact between particles and reduces the tortuosity for ion conduction.^{45 46} Famprakis and coworkers demonstrated that applying pressure during measurement on non-ball-milled (non-BM) Na_3PS_4 improved its observable conductivity by a factor of \sim 10 so that it matched the conductivity of ball milled (BM) Na_3PS_4 .⁴⁶ In contrast, applying pressure on the BM- Na_3PS_4 sample had a negligible effect on its conductivity. They concluded that the better conductivity of BM- Na_3PS_4 was a consequence of better compression/consolidation of the BM- Na_3PS_4 pellets used for EIS measurements.⁴⁶ Inspired by this study, we investigated the conductivity of LNCI-I and LNCI-I-BM under pressure. We found that the conductivity of LNCI-I increased by a factor of \sim 2 (Figure 3c). In contrast, the ion conductivity of LNCI-I-BM hardly improved when applying pressure. We thus observe a similar trend to Famprakis and coworkers and explain our results as follows. For LNCI-I leeway for better consolidation was available and we observed an increase in conductivity when applying pressure. For the LNCI-I-BM sample, the conductivity hardly improved because the smaller particle size enabled near-optimal

consolidation during pelletization. However, two observations indicate that the improved conductivity of LNCI-I-BM is not solely a consequence of better consolidation. (i) Despite the pressure-induced conductivity improvement of LNCI-I by a factor of 2, even under pressure, the conductivity of LNCI-I-BM is still higher by a factor of 5. (ii) An improved conductivity solely originating from superior consolidation would not be expected to show a change in activation energy but the Arrhenius fits in Figure 3b clearly show that the activation energy for LNCI-I-BM is decreased by 40 meV as compared to LNCI-I.

Interestingly the Arrhenius prefactor of LNCI-I-BM is hardly larger than for LNCI-I. For LNCI-I-BM we obtain $\log_{10}(\sigma_0 / \text{S cm}^{-1}) = 2.22$ and for LNCI-I $\log_{10}(\sigma_0 / \text{S cm}^{-1}) = 2.05$. The Arrhenius prefactor comprises factors such as the charge-carrier concentration, the attempt frequency, the jump distance and the correlation factor. These factors are thus only slightly modified by milling and the improved RT conductivity of LNCI-I-BM is predominantly a consequence of the decreased (macroscopic) activation energy. The origin of the reduced macroscopic activation energy of LNCI-I-BM is not entirely understood. Previous studies suggested that amorphous fractions in SEs introduced by high-energy milling may reduce the macroscopic activation energy and consequently improve ion conductivity.^{42 47 48} It was equally suggested that surface-related regions show faster ion diffusion due to increased structural disorder. An increased volume fraction of surface-related regions (concomitant with smaller particle size) may thus enhance bulk diffusion in nanocrystalline ceramics.^{42 47 49}

The activation energy of LNCI-I-BM obtained from a Hendrickson-Bray fit of the ⁷Li NMR lineshape narrowing profile is increased by 20 meV as compared to LNCI-I. This may suggest an increased activation barrier in LNCI-I-BM for the fast, locally confined Li diffusion probed by NMR. However, the accuracy of activation energies obtained from motional narrowing data relies on highly precise line-width measurements. Small errors in the line-width measurements may largely impact the fit result, so that the uncertainty in activation energies obtained by this method typically amounts to a few tens of meV.⁵⁰ This argument is visualized in Figure 3d where a fit line obtained from a H.B.-fit with E_a as a fixed parameter set to 0.22 eV shows a good fit for the narrowing profile of LNCI-I and LNCI-I-BM .

To investigate the effects of further annealing on LNCI-I-BM we re-annealed LNCI-I-BM at 600°C for 3h and subsequent air-quenching restored the initial crystallinity of LNCI-I and the conductivity was reduced to $1 \cdot 10^{-3}$ mS cm⁻¹. Annealing LNCI-I-BM also increased the activation energy to 0.486 ± 0.005 eV which is close to the LNCI-I value of 0.471 ± 0.005 eV (Figure S7). We thus conclude that the beneficial effects of mechanochemical milling on LNCI-I are reversed when annealing the ball milled samples. This result

supports that the reduced particle size and the increased strain obtained after milling LNCl-I may potentially explain the increased Li conductivity of LNCl-I-BM.

Finally we report that LNCl can be synthesized directly via a mechanochemical route without any annealing step. After milling stoichiometric amounts of LiCl and Li₃N for 10 h at 600 rpm LNCl was obtained (Figure S7). Samples synthesized in this way are referred to as BM-LNCl. The RT conductivity of BM-LNCl was found to be 0.015 mS cm⁻¹ and is the highest conductivity ever reported for LNCl. The activation energy of this sample is 0.416 ± 0.005 eV. Analogously to LNCl-I-BM, the conductivity of BM-LNCl is reduced to 5·10⁻³ mS cm⁻¹ after annealing and the activation energy is increased to 0.466 ± 0.005 eV which are values comparable to well consolidated LNCl-I (Figure S7).

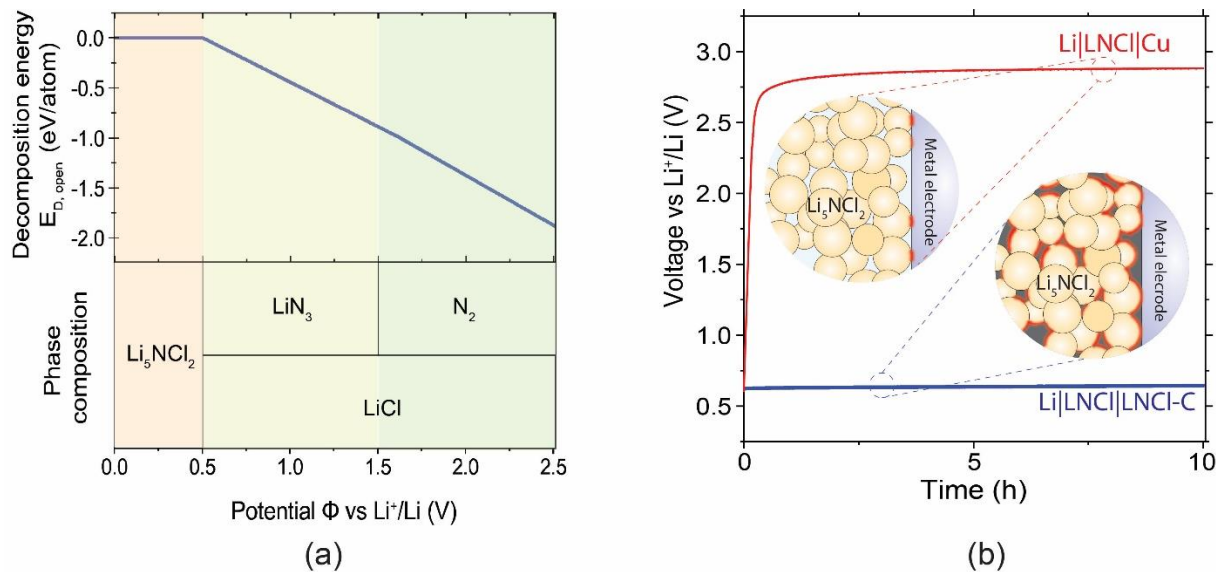


Figure 4. a) Phase equilibria of the $\text{Li}_x\text{NCl}_2 \{x \in \mathbb{R} | x \geq 0\}$ phase space at different potentials ϕ vs Li^+/Li . Additionally this figure shows the decomposition energy $E_{D,\text{open}}$ as defined by Zhu and Mo⁵¹ of LNCl at different ϕ . b) Galvanostatic oxidation of a composite LNCl-C cathode and of LNCl in contact with an ion-blocking Cu disk. The two schematics represent the cathode compositions. In the case of LNCl-C composite cathodes the contact area with the electronic network is much larger as sketched by the red highlighting. The constant current for both curves in b was 0.5 μA (0.64 $\mu\text{A cm}^{-2}$).

Electrochemical stability window of LNCl. The anodic limit of LNCl was previously found to be > 2 V vs (Li^+/Li).¹³ Figure 4a shows the results of our electrochemical stability calculations for LNCl, which were obtained by constructing grand potential diagrams at different chemical potentials of Li (μ_{Li}) leveraging the materials project data base.^{51 52} Our calculations predict that LNCl is thermodynamically stable against Li metal and has an anodic limit of 0.50 V vs (Li^+/Li). Beyond 0.5 V, LNCl was predicted to decompose to lithium azide (LiN_3) and LiCl (Figure 4a)

Overestimated anodic limits for SE were recently often reported.^{53 54} It was previously shown that employing SE-carbon composite electrode in a Li|SE|SE-C cell instead of a simple ion-blocking metal (M) electrode in a Li|SE|M cell, enabled a more accurate measurement of the anodic limit of SEs.^{53 54} The anodic limits obtained when using composite SE-C electrodes are typically significantly lower than the anodic limits obtained with ion-blocking metal electrodes. The smaller anodic limit measured, is a consequence of the increased electrochemical surface area in a SE-C composite electrode; this increases the current signal at the onset of oxidation making the onset of oxidation better observable.^{53 54} Figure 4b shows the galvanostatic charge of a Li|LNCl|LNCl-C cell with an extremely low current of 0.5 μ A (0.64 μ A cm⁻²). The current onset at 0.62 V indicated an experimental anodic limit of 0.62 V for LNCl which is in much closer agreement with the calculated value of 0.50 V than the previous experimental values of >2 V. We repeated the same experiment with a Li|LNCl|Cu cell equally shown in Figure 4b; for this cell the voltage stabilized at 2.7 V and may explain the overestimate in previous reports.

The predicted oxidation of LNCl to LiN₃ calculated to occur at 0.50 V may potentially be kinetically inhibited even at very slow currents because LiN₃ formation necessitates a complex anionic rearrangement to form the [N₃]⁻ moieties present in azides. Such complex anionic rearrangements are additionally hampered by the likely limited RT diffusivity of Cl⁻/N³⁻ in LNCl. In the potential scenario of kinetically inhibited LiN₃ formation the calculated anodic decomposition voltage would be extended from 0.50 V to 0.63 V vs (Li⁺/Li) (Figure S8), which is even closer to our experimental value of ~0.6 V. In principle, the cathodic limit of SEs can be measured in an analogous way to the anodic limit. However, the use of composite SE-C electrodes makes it difficult to distinguish between the lithiation of carbon additives and the lithiation of the SE at potentials close to 0 V vs Li⁺/Li.⁵⁵ Hartwig and coworkers reported chemical stability of LNCl against LM.⁵⁶ This stability was investigated by dipping LNCl into molten Li and the absence of any observed reaction.⁵⁶ We repeated this experiment keeping LNCl powder submerged in molten Li at 210 °C for 2h. No new peaks were observed after this in our XRD experiments (Figure S9). Additionally symmetric Li|LNCl|Li cells display flat stripping/plating plateaus and no increase in the cell voltage (Figure S9) over time, indicating a stable LM/LNCl interface.

Based on our findings on LNCl it convenes to reflect on its applicability in ASSBs. A key property of LNCl is its thermodynamic stability against LM which is uncommon for SEs. However, its low anodic limit (~0.6 V) inhibits its application in combination with common high-voltage cathodes and confines the applicability of LNCl to an artificial buffer layer between LM and alternative SEs that face the cathode. In such a hybrid

bilayer SE architecture, LNCI would be in close contact with a partner SE. The realization of such systems thus hinges on the chemical compatibility between LNCI and other common SEs.

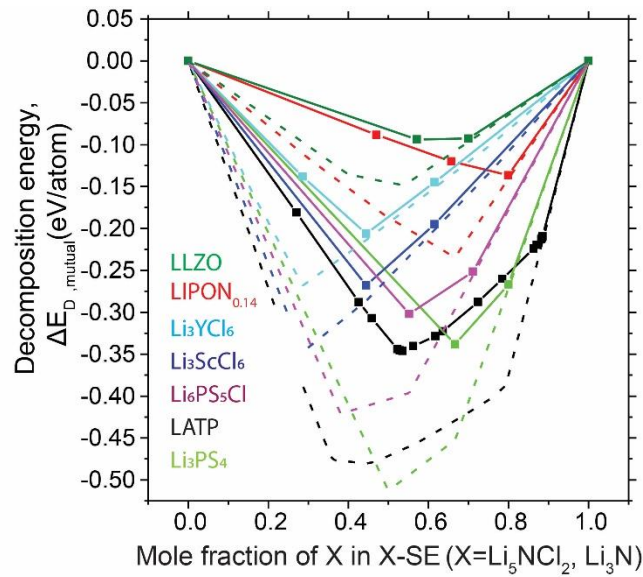


Figure 5. Pseudo-binaries between LNCI/Li₃N and common highly-conducting SEs. The solid lines are pseudo-binaries between LNCI and different SEs and the dashed lines are for pseudo-binaries between Li₃N and different SEs

We investigated the thermodynamic driving force of LNCI to chemically react with common SEs by constructing pseudo-binaries in phase space (Figure 5) leveraging the materials project database, as explained in detail elsewhere.⁵¹ Figure 5 shows the pseudo binaries between LNCI and different SEs. $\Delta E_{D, \text{mutual}}$ as defined by Zhu and Mo⁵¹ is the reaction energy for the reaction between LNCI and the SE of interest. We would like to highlight that a thermodynamic driving force for chemical reaction ($\Delta E_{D, \text{mutual}} < 0$) between two SEs does not necessarily imply immediate reaction upon contact; the diffusivity of elements in Li⁺-conducting SEs (excluding Li⁺) is limited at ambient temperatures so that an immediate solid-state reaction upon contact may be kinetically inhibited. $\Delta E_{D, \text{mutual}}$ can be treated as a propensity for reaction especially if the hybrid bilayer electrolyte is subjected to annealing/heating steps.⁵¹

Figure 5 shows that LNCI has the strongest propensity for chemical decomposition with LATP and sulfide-based SEs such as the argyrodite Li₆PS₅Cl and Li₃PS₄. With halide (Li₃MCl₆) electrolytes the decomposition energy is reduced and seems to be mainly driven by the formation of strong M³⁺-N³⁻ bonds. The decomposition energy $\Delta E_{D, \text{mutual}}$ of Li₃ScCl₆ is 100 meV/atom larger than for Li₃YCl₆ which can be explained by a stronger Sc-N affinity compared to Y-N. The propensity for chemical decomposition is further reduced between LNCI and LIPON-type electrolytes and the garnet (LLZO) electrolyte. Figure 5 equally shows the pseudo-binaries of Li₃N and the SEs of interest (dashed lines). α -Li₃N has a larger ion conductivity than

LNCl ($0.1\text{--}1 \text{ mS cm}^{-1}$)^{57 58} and is equally thermodynamically stable against Li metal.⁵⁷ Similar to LNCl, the applicability of α -Li₃N is confined by its limited anodic limit (0.44 V).^{57 59} However, the driving force for chemical decomposition with common SEs is larger with Li₃N by 50 - 200 eV/atom than with LNCl. This suggests a stronger propensity for decomposition at the Li₃N|SE interface than at the LNCl|SE interface. Hybrid bilayer electrolytes are scarcely investigated but bear the potential to enable ASSBs.⁶⁰ Beyond good ion conductivity ($\sim 0.1 \text{ mS cm}^{-1}$), the anolyte needs to balance chemical stability, contact stability and lithium dendrite suppression on the LM side and compatibility with the catholyte. This complex interplay of chemical, mechanical and microstructural properties of the anolyte motivates the exploration and optimization of different phases that are thermodynamically stable against LM such as the lithium nitride halides. However, the future practicality of LNCl will depend on whether its practical conductivity can be increased.

Conclusion

We investigated the fundamental Li diffusion mechanism in LNCl using AIMD simulations. We found that Li diffuses through the edge of edge-sharing tetrahedral Li sites. The affinity for jumps between two Li sites depends on the N/Cl-composition of the tetrahedra enclosing the Li sites and of the bottleneck-edge composition. We found that jumps into Cl₄ Li sites and jumps through Cl-Cl edges have the largest $E_{a,\text{jump}}$ values indicating that they are unfavorable compared to other jump events. Our EIS experiments confirmed the previously reported Li conductivity of $1\cdot10^3 \text{ mS cm}^{-1}$ and an E_a of 0.47 eV. Much faster Li motion was detected with ⁷Li NMR ($>0.1 \text{ mS cm}^{-1}$) with a lower $E_a \sim 0.25 \text{ eV}$. We propose that the fast Li motion may arise from readily occurring jumps with low $E_{a,\text{jump}}$ values and that the long-range conductivity probed by EIS is limited by jumps with large $E_{a,\text{jump}}$ values. Introducing a 4h mechanochemical milling step after solid state synthesis improves the RT conductivity of LNCl by an order of magnitude to 0.01 mS cm^{-1} and lowers the activation energy to 0.42 eV. It was shown that LNCl can be synthesized mechanochemically without any annealing step and these samples reached conductivities of 0.015 mS cm^{-1} . Re-annealing of milled LNCl samples at 600 °C eliminates the beneficial effects of milling as the conductivity is reduced and the activation energy increased to values obtained for non-milled samples. Our experiments showed that the anodic limit of LNCl is $\sim 0.6 \text{ V}$ (vs Li⁺/Li) which is significantly lower than the previously reported $>2 \text{ V}$ (vs Li⁺/Li) and matches our first principles thermodynamic calculations. We established that the anodic limit of LNCl confines its potential role in ASSBs to an artificial buffer layer between LM and other highly-conducting SEs where the thermodynamic stability of LNCl against LM may be beneficial. Our calculations show that from a thermodynamic viewpoint, LNCl is chemically better compatible with common highly-conducting SEs than Li₃N. Future investigations on LNCl should focus on

different synthesis approaches of LNCl, how they affect sub-ordering of the N/Cl anionic framework and how this may potentially affect Li ion conductivity. Additionally, doping strategies have previously been investigated³⁵ and should be further explored.

Methodology

Synthesis. *LNCl-I:* The synthesis precursors were LiCl (Sigma-Aldrich, 99%) and Li₃N (Sigma-Aldrich, >99.5%). Stoichiometric amounts of the precursors with 10% wt. excess Li₃N were milled in a planetary ball mill (Jar: ZrO₂, 45 mL) with 10 mm ZrO₂ balls and a ball/powder ratio of 13 at 270 rpm for 4.5 h (5 min milling; 15 min pause) to ensure good mixing of the precursors. Subsequently the precursor mix was pressed into a pellet (1.3 tons) and transferred to an airtight Cu crucible. The crucible was placed in a furnace and heated with a rate of 300°C/h to 600°C, maintained at this temperature for 3 h and then air quenched. *LNCl-I-BM:* To obtain LNCl-I-BM, LNCl-I was transferred to a planetary ball mill (Jar: ZrO₂, 45 mL) with 1 mm ZrO₂ balls and a ball/powder ratio of 25 and milled for 4h (5 min milling; 5 min pause). After each hour of milling, all powder was removed from the inner walls of the jar to ensure effective milling. *BM-LNCl:* Stoichiometric amounts of LiCl and Li₃N with 10% wt. excess Li₃N were milled in a planetary ball mill (Jar: ZrO₂, 45 mL) with 10 mm ZrO₂ balls and a ball/powder ratio of 13 at 600 rpm for 10 h (5 min milling; 5 pause). All preparation steps were done in an argon atmosphere (H₂O < 1 ppm, O₂ < 1 ppm). *LNCl-I in contact with molten Li:* LNCl-I was placed between two LM disks in a W crucible which was sealed in a quartz ampoule. The ampoule was exposed to 210 °C for 2 h and then removed from the furnace.

Electrochemical Characterization. *EIS:* Pellets of the LNCl probes were pressed (3.2 tons) in custom-made solid-state lab cells. The cell configuration was SS|LNCl|SS (SS=stainless steel). AC impedance was performed with an Autolab (AUT86298) in the frequency range 10 MHz to 0.1 Hz with a voltage amplitude of 10 mV. *Galvanostatic measurements:* Galvanostatic measurements were also performed with an Autolab (AUT86298). To measure the anodic limit of LNCl, Li|LNCl-I-BM|LNCl-I-C were used. To make the LNCl-I-C composite cathode a mixture of LNCl-I: Super P:carbon-nanotubes with a weight ratio of 0.7:0.15:0.15 was milled in a planetary ball mill (Jar: ZrO₂, 45 mL) with 10 mm ZrO₂ balls and a ball/powder ratio of 30 at 400 rpm for 2 h (5 min milling; 5 min pause). After the first hour of milling, all powder was removed from the inner walls of the jar to ensure good mixing. Li|LNCl-I-BM|LNCl-I-C cells were assembled by pressing a LNCl-I-BM pellet (130 mg, 3.2 tons) and subsequently the LNCl-I-C composite (15 mg, 3.2 tons) on top of it. Finally a Li disk was pasted on the opposite side of the LNCl-I-BM pellet. LNCl-I-BM was used as the SE because it is 10 times more conductive than LNCl-I so that voltage drops in the SE

becomes negligible (<0.01 V) at the current used 0.5 μ A (0.64 μ A cm⁻²). *Conductivity measurements at different temperatures for Arrhenius fits:* SS|LNCl|SS cells were kept at 30°C for 1h, then heated in 5 min to 50°C and kept at this temperature for 30 min followed by heating to 60°C in 5 min and maintaining the temperature for 30 min. This procedure was continued up to 100°C. The EIS obtained at the end of the 30 min temperature-plateaus were used for Arrhenius fits.

Solid state NMR. Solid state NMR measurements were done on a Bruker Ascend 500 MHz spectrometer with a ⁷Li resonance frequency of 194.381 MHz. The 90° pulse length was typically 2.7-2.8 μ s. Air sensitive LNCl probes were sealed in 4 mm diameter Teflon rotors in an Ar glove box. The variable temperature ⁷Li NMR experiments were conducted statically without MAS in a temperature range from -120°C to 160°C. The chemical shifts were referenced to a 0.1 M aqueous LiCl solution.

X-ray diffraction. Powder diffractograms were collected in the 2 θ range 10 – 100° using Cu K α X-rays (1.54 Å, 45 kV, 40 mA) on a PANalytical X’Pert Pro X-ray diffractometer . The air sensitive LNCl probes were loaded into air-tight holders in an Ar glovebox prior to the measurements. An LaB₆ NIST (NIST660c) standard was employed to calibrate instrumental broadening. The JANA2006 program⁶¹ was used for LeBail and Rietveld refinements and the Williamson-Hall analysis.

Computational details. All DFT calculations were performed with the Vienna ab-initio simulation package VASP with computational settings consistent with those used in the Materials Project database.⁵² Calculations were done on a 2x2x2 LNCl supercell. Because of the partial occupancies in LNCl different atomic arrangements were generated. Starting point was an initial guess of a 2x2x2 supercell with all Li positions occupied (real supercell stoichiometry Li₆₄N₁₁Cl₂₁) the N/Cl arrangement was optimized by minimizing the electrostatic energy using the *OrderDisorderStandardTransformation* tool as implemented in pymatgen.⁶² Subsequently, for the 20 arrangements with the lowest electrostatic energy, 20 further supercells were generated by removing Li, again minimizing the electrostatic energy with the *PartialRemoveSpeciesTranfomation* tool as implemented in pymatgen.⁶² From this pool of 400 supercells, the 40 supercells with the lowest electrostatic energy were relaxed with DFT. Additionally >10 000 supercells were generated randomly. The 40 “random” supercells with the lowest electrostatic energy were relaxed with DFT. The supercell with the lowest internal energy as calculated by DFT was taken and the N/Cl arrangement was re-optimized minimizing the electrostatic energy and the 40 supercells with the lowest electrostatic energy were relaxed with DFT. Of all supercells generated, the supercell with the lowest internal energy as calculated by DFT was adopted as the model supercell. The stoichiometry of the supercells was always Li_{4.82}NCl_{1.91} (Li₅₃N₁₁Cl₂₁) and approximates the Li₅NCl₂ (Li_{53.333}N_{10.666}Cl_{21.333})

stoichiometry as good as possible given the supercell-size constraints in AIMD simulations. The electrochemical stability window and the pseudo-binaries were calculated as described in the work by Zhu and Mo.⁵¹ For the pseudo-binaries, the SE phase compositions with energies above the hull set to zero were added to the materials project phase space. Subsequently $E_{D, \text{mulutal}}$ as defined by Zhu and Mo⁵¹ was calculated between LNCl and respective SEs. AIMD simulations were done in the NVT ensemble and with 2 fs time steps. The kpoint grid used was 1x1x1 and the energy cutoff was 400 eV. For the AIMD simulations the Li pseudopotential was changed from Li_sv (which was used for relaxations) to Li as this enables the use of a lower energy cutoff. The simulation time was > 200 ps for every AIMD simulation and the error on the obtained diffusivities was estimated as done by He and Mo.³³ The dissection of AIMD simulations into individual jump events and subsequent analysis of the prefactor frequency, jump-diffusivity, jump frequencies and individual $E_{a, \text{Jump}}$ values was done as first described by de Klerk and Wagemaker,²⁸ a comprehensive account can be found in ref 28 but crucial aspects for the understanding of the reported data is presented here. *Calculation of $E_{a, \text{jump}}$ values between two sites:* The sites are defined around the 0 K equilibrium positions of the Li ions. At every simulation step it is recorded in which site each Li ions is located or whether it is currently between two sites. From this information the jump frequency between two site $v_{A \rightarrow B}$ can be calculated according to equation 8:

$$v_{A \rightarrow B} = \frac{N_{A \rightarrow B}}{\tau_A} \quad (8)$$

where $v_{A \rightarrow B}$ is the jump frequency for jumps from site A to site B, $N_{A \rightarrow B}$ is the number of recorded jumps from A to B, and τ_A is the time of occupation of site A. $E_{a, \text{jump}}$ is then obtained from equation (1). *Calculation of Jump diffusivities and tracer diffusivities D_J and D_{tr} :* D_J and D_{tr} are in principle calculated with the same formula:

$$D = \frac{\langle x^2 \rangle}{2dt} \quad (9)$$

Where $\langle x^2 \rangle$ is the mean square displacement of the lithium ions, d the dimensionality of diffusion and t the simulation time. D_J and D_{tr} differ in the way $\langle x^2 \rangle$ is calculated. For D_{tr} , $\langle x^2 \rangle$ is directly obtained from the AIMD simulation. For D_J , $\langle x^2 \rangle$ is calculated by summing up the jump-distances and averaging over the number of Li ions:

$$\langle x^2 \rangle_{\text{for } D_J} = \frac{1}{N} \sum_{i=1}^M a_i^2 \quad (10)$$

where N is the total number of diffusing ions and $a_{A \rightarrow B}$ the jump distance of a generalized jump-event “i” and M the total number of jumps observed. Combining equations (9) and (10) yields equation (4). *Calculation of the relative site energies:* LNCI intrinsically contains Li vacancies. The site-energy difference between a site A and a site B was obtained by displacing a Li in site A to an empty site B. The energy difference between the two supercells was interpreted as the site-energy difference between sites A and B. The average site-energy difference between sites A and B was calculated from 10 such displacements.

- (1) Berg, E. J.; Villevieille, C.; Streich, D.; Trabesinger, S.; Novák, P. Rechargeable Batteries: Grasping for the Limits of Chemistry. *J. Electrochem. Soc.* **2015**, *162* (14), A2468–A2475.
- (2) Cao, D.; Sun, X.; Li, Q.; Natan, A.; Xiang, P.; Zhu, H. Lithium Dendrite in All-Solid-State Batteries: Growth Mechanisms, Suppression Strategies, and Characterizations. *Matter* **2020**, *3* (1), 57–94.
- (3) Janek, J.; Zeier, W. G. A Solid Future for Battery Development. *Nat. Energy* **2016**, *1* (9), 1–4.
- (4) Park, K. H.; Bai, Q.; Kim, D. H.; Oh, D. Y.; Zhu, Y.; Mo, Y.; Jung, Y. S. Design Strategies, Practical Considerations, and New Solution Processes of Sulfide Solid Electrolytes for All-Solid-State Batteries. *Adv. Energy Mater.* **2018**, *8* (18), 1–24.
- (5) Abakumov, A. M.; Fedotov, S. S.; Antipov, E. V.; Tarascon, J. M. Solid State Chemistry for Developing Better Metal-Ion Batteries. *Nat. Commun.* **2020**, *11* (1), 1–14.
- (6) Famprakis, T.; Canepa, P.; Dawson, J. A.; Islam, M. S.; Masquelier, C. Fundamentals of Inorganic Solid-State Electrolytes for Batteries. *Nat. Mater.* **2019**, *18*.
- (7) Zhang, Z.; Shao, Y.; Lotsch, B.; Hu, Y. S.; Li, H.; Janek, J.; Nazar, L. F.; Nan, C. W.; Maier, J.; Armand, M.; Chen, L. New Horizons for Inorganic Solid State Ion Conductors. *Energy Environ. Sci.* **2018**, *11* (8), 1945–1976.
- (8) Rieger, L. M.; Schlem, R.; Sann, J.; Zeier, W. G.; Janek, J. Lithium-Metal Anode Instability of the Superionic Halide Solid Electrolytes and the Implications for Solid-State Batteries. *Angew. Chemie* **2021**, *133* (12), 6792–6797.
- (9) Monroe, C.; Newman, J. The Impact of Elastic Deformation on Deposition Kinetics at Lithium/Polymer Interfaces. *J. Electrochem. Soc.* **2005**, *152* (2), A396.
- (10) Ahmad, Z.; Viswanathan, V. Stability of Electrodeposition at Solid-Solid Interfaces and Implications for Metal Anodes. *Phys. Rev. Lett.* **2017**, *119* (5), 1–6.
- (11) Porz, L.; Swamy, T.; Sheldon, B. W.; Rettenwander, D.; Frömling, T.; Thaman, H. L.; Berendts, S.; Uecker, R.; Carter, W. C.; Chiang, Y. M. Mechanism of Lithium Metal Penetration through Inorganic Solid Electrolytes. *Adv. Energy Mater.* **2017**, *7* (20), 1–12.

- (12) Yu, S.; Schmidt, R. D.; Garcia-Mendez, R.; Herbert, E.; Dudney, N. J.; Wolfenstine, J. B.; Sakamoto, J.; Siegel, D. J. Elastic Properties of the Solid Electrolyte Li₇La₃Zr₂O₁₂ (LLZO). *Chem. Mater.* **2016**, *28* (1), 197–206.
- (13) Weppner, W.; Hartwig, P.; Rabenau, A. Consideration of Lithium Nitride Halides as Solid Electrolytes in Practical Galvanic Cell Applications. *J. Power Sources* **1981**, *6* (3), 251–259.
- (14) Marx, R. Preparation and Crystal Structure of Lithium Nitride Chloride Li₄NCl. *J. Solid State Chem.* **1997**, *128* (2), 241–246.
- (15) Marx, R.; Mayer, H. M. Preparation and Crystal Structure of Ordered and Disordered Lithium Nitride Dichloride, Li₅NCl₂. *J. Solid State Chem.* **1997**, *130* (1), 90–96.
- (16) Marx, R.; Mayer, H. M. Reindarstellung Und Kristallstruktur von Lithiumnitriddibromid, Li₅NBr₂. *Zeitschrift fur Naturforsch. - Sect. B J. Chem. Sci.* **1995**, *50* (9), 1353–1358.
- (17) Marx, R.; Mayer, H.-M. Darstellung Und Lithiumteilstruktur von Lithiumnitridtribromid, Li₆NBr₃ Und Lithiumnitridtriiodid, Li₆NI₃. *Z. Naturforsch.* **1996**, *3*, 525–530.
- (18) Galvez-Aranda, D. E.; Seminario, J. M. Ab Initio Study of the Interface of the Solid-State Electrolyte Li₉N₂Cl₃ with a Li-Metal Electrode . *J. Electrochem. Soc.* **2019**, *166* (10), A2048–A2057.
- (19) Sang, J.; Yu, Y.; Wang, Z.; Shao, G. Theoretical Formulation of Li₃: A + BN_xb(X = Halogen) as a Potential Artificial Solid Electrolyte Interphase (ASEI) to Protect the Li Anode. *Phys. Chem. Chem. Phys.* **2020**, *22* (23), 12918–12928.
- (20) Bruce, P. G. *Solid State Electrochemistry*; Cambridge university press, 1997.
- (21) Halogenide, T.; Chloride, T.; Lithium, D. S.; Synthese, S.; Ionenbewegung, K.; Bohnsack, A.; Stenzel, F.; Zajonc, A.; Balzer, G.; Wickleder, M. S.; Synthesis, S.; Structures, C.; Motion, I. *Zeitschrift Fur Anorganische Und Allgemeine Chemie Ternary Halides of the A₃MX₆ Type . VI .* **1997**, *623*, 1067–1073.
- (22) Li, X.; Liang, J.; Yang, X.; Adair, K. R.; Wang, C.; Zhao, F.; Sun, X. Progress and Perspectives on Halide Lithium Conductors for All-Solid-State Lithium Batteries. *Energy Environ. Sci.* **2020**, *13* (5), 1429–1461.
- (23) Asano, T.; Sakai, A.; Ouchi, S.; Sakaida, M.; Miyazaki, A.; Hasegawa, S. Solid Halide Electrolytes with High Lithium-Ion Conductivity for Application in 4 V Class Bulk-Type All-Solid-State Batteries. *Adv. Mater.* **2018**, *30* (44), 1–7.
- (24) Mo, Y.; Ong, S. P.; Ceder, G. First Principles Study of the Li₁₀GeP₂S₁₂ Lithium Super Ionic Conductor Material. *Chem. Mater.* **2012**, *24* (1), 15–17.
- (25) Han, F.; Zhu, Y.; He, X.; Mo, Y.; Wang, C. Electrochemical Stability of Li₁₀GeP₂S₁₂ and Li₇La₃Zr₂O₁₂ Solid Electrolytes. *Adv. Energy Mater.* **2016**, *6* (8), 1–9.
- (26) Liu, Y.; Wang, S.; Nolan, A. M.; Ling, C.; Mo, Y. Tailoring the Cation Lattice for Chloride Lithium-Ion Conductors. *Adv. Energy Mater.* **2020**, *10* (40), 1–11.

- (27) He, X.; Mo, Y. Accelerated Materials Design of Na_{0.5}Bi_{0.5}TiO₃ Oxygen Ionic Conductors Based on First Principles Calculations. *Phys. Chem. Chem. Phys.* **2015**, *17* (27), 18035–18044.
- (28) De Klerk, N. J. J.; Van Der Maas, E.; Wagemaker, M. Analysis of Diffusion in Solid-State Electrolytes through MD Simulations, Improvement of the Li-Ion Conductivity in β -Li₃PS₄ as an Example. *ACS Appl. Energy Mater.* **2018**, *1* (7), 3230–3242.
- (29) Yu, C.; Ganapathy, S.; De Klerk, N. J. J.; Roslon, I.; Van Eck, E. R. H.; Kentgens, A. P. M.; Wagemaker, M. Unravelling Li-Ion Transport from Picoseconds to Seconds: Bulk versus Interfaces in an Argyrodite Li₆PS₅Cl-Li₂S All-Solid-State Li-Ion Battery. *J. Am. Chem. Soc.* **2016**, *138* (35), 11192–11201.
- (30) Chen, F.; Xu, L.; Li, J.; Yang, Y.; Shen, Q. Effect of Bottleneck Size on Lithium Migration in Lithium Garnets Li₇La₃Zr₂O₁₂ (LLZO). *Ionics (Kiel)*. **2020**, *26* (6), 3193–3198.
- (31) Fu, Z. H.; Chen, X.; Zhao, C. Z.; Yuan, H.; Zhang, R.; Shen, X.; Ma, X. X.; Lu, Y.; Liu, Q. B.; Fan, L. Z.; Zhang, Q. Stress Regulation on Atomic Bonding and Ionic Diffusivity: Mechanochemical Effects in Sulfide Solid Electrolytes. *Energy and Fuels* **2021**, *35* (12), 10210–10218.
- (32) Shannon, R. D. Revised Effective Ionic Radii and Systematic Studies of Interatomic Distances in Halides and Chalcogenides. *Acta Crystallogr. Sect. A Cryst. physics, diffraction, Theor. Gen. Crystallogr.* **1976**, *32* (5), 751–767.
- (33) He, X.; Zhu, Y.; Epstein, A.; Mo, Y. Statistical Variances of Diffusional Properties from Ab Initio Molecular Dynamics Simulations. *npj Comput. Mater.* **2018**, *4* (1).
- (34) Tilley, R. J. D. *Defects in Solids*; John Wiley & Sons, 2008.
- (35) Jia, Y.; Yang, J. Study of the Lithium Solid Electrolytes Based on Lithium Nitride Chloride (Li₉N₂Cl₃). *Solid State Ionics* **1997**, *96* (1–2), 113–117.
- (36) Hartwig, P.; Rabenau, A.; Weppner, W. Phase Equilibria and Theromdynamic Properties of the Li-N-Cl, Li-N-Br and Li-N-I Systems. *1981*, *80*, 81–90.
- (37) Sattlegger, H.; Hahn, H. Über Das System Li₃N/LiCl. *Zeitschrift für Anorg. und Allg. Chemie* **1971**, *379* (3), 293–299.
- (38) Brug, G. J.; van den Eeden, A. L. G.; Sluyters-Rehbach, M.; Sluyters, J. H. The Analysis of Electrode Impedances Complicated by the Presence of a Constant Phase Element. *J. Electroanal. Chem.* **1984**, *176* (1–2), 275–295.
- (39) Hirschorn, B.; Orazem, M. E.; Tribollet, B.; Vivier, V.; Frateur, I.; Musiani, M. Determination of Effective Capacitance and Film Thickness from Constant-Phase-Element Parameters. *Electrochim. Acta* **2010**, *55*, 6218–6227.
- (40) West, A.; Irvine, J.; Sinclair, D. Electroceramics : Characterization by Impedance Spectroscopy. *Adv. Mater.* **1990**, *2* (3), 132–138.

- (41) Epp, V.; Wilkening, M. Li-Ion Dynamics in Solids as Seen Via Relaxation NMR. In *Handbook of Solid State Batteries*; 2016; pp 133–190.
- (42) Brinek, M.; Hiebl, C.; Wilkening, H. M. R. Understanding the Origin of Enhanced Li-Ion Transport in Nanocrystalline Argyrodite-Type Li₆PS₅I. *Chem. Mater.* **2020**, *32* (11), 4754–4766.
- (43) Hendrickson, J. R.; Bray, P. J. A Phenomenological Equation for NMR Motional Narrowing in Solids. *J. Magn. Reson.* **1973**, *9* (3), 341–357.
- (44) Waugh, J.; Fedin, E. No Title. *Sov. Phys. Solid State* **1963**, *16* (3).
- (45) Schlem, R.; Burmeister, C. F.; Michalowski, P.; Ohno, S.; Dewald, G. F.; Kwade, A.; Zeier, W. G. Energy Storage Materials for Solid-State Batteries: Design by Mechanochemistry. *Adv. Energy Mater.* **2021**, *11* (30).
- (46) Famprakis, T.; Kudu, O. U.; Dawson, J. A.; Canepa, P.; Fauth, F.; Suard, E.; Zbiri, M.; Dambournet, D.; Borkiewicz, O. J.; Bouyanfif, H.; Emge, S. P.; Cretu, S.; Chotard, J. N.; Grey, C. P.; Zeier, W. G.; Islam, M. S.; Masquelier, C. Under Pressure: Mechanochemical Effects on Structure and Ion Conduction in the Sodium-Ion Solid Electrolyte Na₃PS₄. *J. Am. Chem. Soc.* **2020**, *142* (43), 18422–18436.
- (47) Wilkening, M.; Bork, D.; Indris, S.; Heijmans, P. Diffusion in Amorphous LiNbO₃ Studied by ⁷Li NMR - Comparison with the Nano- and Microcrystalline Material. *Phys. Chem. Chem. Phys.* **2002**, *4* (14), 3246–3251.
- (48) Boulineau, S.; Courty, M.; Tarascon, J. M.; Viallet, V. Mechanochemical Synthesis of Li-Arnyrodite Li₆PS₅X (X = Cl, Br, I) as Sulfur-Based Solid Electrolytes for All Solid State Batteries Application. *Solid State Ionics* **2012**, *221*, 1–5.
- (49) Breuer, S.; Uitz, M.; Wilkening, H. M. R. Rapid Li Ion Dynamics in the Interfacial Regions of Nanocrystalline Solids. *J. Phys. Chem. Lett.* **2018**, *9* (8), 2093–2097.
- (50) Kuhn, A.; Narayanan, S.; Spencer, L.; Goward, G.; Thangadurai, V.; Wilkening, M. Li Self-Diffusion in Garnet-Type Li₇La₃Zr₂O₁₂ as Probed Directly by Diffusion-Induced Li⁷ Spin-Lattice Relaxation NMR Spectroscopy. *Phys. Rev. B - Condens. Matter Mater. Phys.* **2011**, *83* (9), 1–11.
- (51) Zhu, Y.; He, X.; Mo, Y. First Principles Study on Electrochemical and Chemical Stability of Solid Electrolyte-Electrode Interfaces in All-Solid-State Li-Ion Batteries. *J. Mater. Chem. A* **2016**, *4* (9), 3253–3266.
- (52) Jain, A.; Ong, S. P.; Hautier, G.; Chen, W.; Richards, W. D.; Dacek, S.; Cholia, S.; Gunter, D.; Skinner, D.; Ceder, G.; Persson, K. A. Commentary: The Materials Project: A Materials Genome Approach to Accelerating Materials Innovation. *APL Mater.* **2013**, *1* (1).
- (53) Han, F.; Zhu, Y.; He, X.; Mo, Y.; Wang, C. Electrochemical Stability of Li₁₀GeP₂S₁₂ and Li₇La₃Zr₂O₁₂ Solid Electrolytes. *Adv. Energy Mater.* **2016**, *6* (8).
- (54) Schwietert, T. K.; Arszelewska, V. A.; Wang, C.; Yu, C.; Vasileiadis, A.; J Klerk, N. J.;

- Hageman, J.; Hupfer, T.; Kerkamm, I.; Xu, Y.; Maas, E.; Kelder, E. M.; Ganapathy, S.; Wagemaker, M. Clarifying the Relationship between Redox Activity and Electrochemical Stability in Solid Electrolytes. *Nat. Mater.* **2020**, *19* (4), 428–435.
- (55) Peng, B.; Xu, Y.; Wang, X.; Shi, X.; Mulder, F. M. The Electrochemical Performance of Super P Carbon Black in Reversible Li/Na Ion Uptake. *Sci. China Physics, Mech. Astron.* **2017**, *60* (6).
- (56) Hartwig, P.; Weppner, W.; Wichelhaus, W. Fast Ionic Lithium Conduction in Solid Lithium Nitride Chloride. *Mat. Res. Bull.* **1979**, *14*, 493–498.
- (57) Alpen, U. v. Li₃N: A Promising Li Ionic Conductor. *J. Solid State Chem.* **1979**, *29* (3), 379–392.
- (58) Boukamp, B. A.; Huggins, R. A. Lithium Ion Conductivity in Lithium Nitride. *Phys. Lett. A* **1976**, *58* (4), 231–233.
- (59) Rea, J. R.; Foster, D. L.; Mallory, P. R.; Co. Inc. High Ionic Conductivity in Densified Polycrystalline Lithium Nitride. *Mater. Res. Bull.* **1979**, *14* (6), 841–846.
- (60) Weiss, M.; Simon, F. J.; Busche, M. R.; Nakamura, T.; Schröder, D.; Richter, F. H.; Janek, J. From Liquid- to Solid-State Batteries: Ion Transfer Kinetics of Heteroionic Interfaces. *Electrochem. Energy Rev.* **2020**, *3* (2), 221–238.
- (61) Petříček, V.; Dušek, M.; Palatinus, L. Crystallographic Computing System JANA2006: General Features. *Zeitschrift für Krist. - Cryst. Mater.* **2014**, *229* (5), 345–352.
- (62) Ong, S. P.; Richards, W. D.; Jain, A.; Hautier, G.; Kocher, M.; Cholia, S.; Gunter, D.; Chevrier, V. L.; Persson, K. A.; Ceder, G. Python Materials Genomics (Pymatgen): A Robust, Open-Source Python Library for Materials Analysis. *Comput. Mater. Sci.* **2013**, *68*, 314–319.

Supporting Information